Adaptive centroid-finding algorithm for freeform surface measurements

Guo, Wenjiang; Zhao, Liping; Tong, Chin Shi; Chen, I-Ming; Joshi, Sunil Chandrakant

2013

Guo, W., Zhao, L., Tong, C. S., Chen, I.-M., & Joshi, S. C. (2013). Adaptive centroid-finding algorithm for freeform surface measurements. Applied Optics, 52(10), D75-D83.

https://hdl.handle.net/10356/96108

https://doi.org/10.1364/AO.52.000D75

Adaptive centroid-finding algorithm for freeform surface measurements

Wenjiang Guo,[1,2,*] Liping Zhao,[1] Chin Shi Tong,[2] Chen I-Ming,[2] and Sunil Chandrakant Joshi[2]

[1]Optical Metrology Group, National Metrology Center (NMC), 1 Science Park Drive, Singapore 118221

[2]School of Mechanical and Aerospace Engineering, Nanyang Technological University, 50 Nanyang Avenue, Singapore 639798

*Corresponding author: wjguo.student@simtech.a-star.edu.sg

Received 28 November 2012; revised 1 February 2013; accepted 21 February 2013; posted 22 February 2013 (Doc. ID 180777); published 27 March 2013

Wavefront sensing systems measure the slope or curvature of a surface by calculating the centroid displacement of two focal spot images. Accurately finding the centroid of each focal spot determines the measurement results. This paper studied several widely used centroid-finding techniques and observed that thresholding is the most critical factor affecting the centroid-finding accuracy. Since the focal spot image of a freeform surface usually suffers from various types of image degradation, it is difficult and sometimes impossible to set a best threshold value for the whole image. We propose an adaptive centroid-finding algorithm to tackle this problem and have experimentally proven its effectiveness in measuring freeform surfaces. © 2013 Optical Society of America

OCIS codes: 100.0100, 100.3010, 010.7350.

1. Introduction

Freeform surfaces are increasingly used in industry and in various applications because of their reduced geometrical aberrations, reduced complexity, reduced system size and weight, and greater design flexibility [1]. Such surfaces are challenging to manufacture and to measure, and their function is, by definition, profoundly affected by their geometrical characteristics. To address this problem, a noncontact, freeform measurement is needed. [2].

Some of the well-known noncontact optical surface measurement techniques are interferometry, confocal microscopy, Moiré fringe projection, and the Shack–Hartmann wavefront sensing (SHWS) [3] technique. Except for confocal microscopy, the other three techniques are area-based, which require less measurement time and avoid errors due to temperature variations and vibration during the measurement. While the height accuracy achievable by the Moiré fringe projection is within tens of microns, interferometry and SHWS can achieve accuracies within the nano scale [4]. Hence, only interferometry and SHWS are considered for the intended application.

Interferometry is sensitive to vibration, requires a coherent light source, and has limited dynamic range. Although computer-generated hologram has made testing of aspheric surfaces possible, it is expensive as the null lens must be specially designed and manufactured for each specific surface shape [5]. Therefore, interferometry is mostly used for flatness measurement, and is not applicable for *in situ* operation. On the contrary, SHWS is insensitive to vibration and there is no need for a coherent light source [6]. Furthermore, much progress has been made to increase its dynamic range [7,8], while achieving the same vertical accuracy as interferometry. In addition, an extended version, called the reference-free wavefront sensing [9] technique, allows the measurement of a wavefront without involving a reference piece which makes freeform surface

1559-128X/13/100D75-09$15.00/0

measurement more feasible. Because of these characteristics, SHWS is promising for freeform surface measurements compared to other noncontact optical surface measurement techniques.

Because the SHWS reconstruction relies on the centroid displacement, its accuracy is significantly dependent on the technique used to determine the centroid positions [10]. The most commonly adopted method is the first moment algorithm (FMM), which calculates the centroid position of each window by Eq. (1):

$$X_C = \frac{\sum_{i=1}^{M}\sum_{j=1}^{N} X_i I(X_i, Y_j)}{\sum_{i=1}^{M}\sum_{j=1}^{N} I(X_i, Y_j)}$$
$$Y_C = \frac{\sum_{i=1}^{M}\sum_{j=1}^{N} Y_j I(X_i, Y_j)}{\sum_{i=1}^{M}\sum_{j=1}^{N} I(X_i, Y_j)}. \quad (1)$$

This algorithm is impractical for real cases because its consistency is severely limited by background and photon noise [11,12], especially if the signal spot is smaller than the subaperture window [10–12]. Supplementary techniques have been introduced to significantly improve the FMM centroid detection accuracy: thresholding, high power, subwindowing, and iteration [11–14]. However, these techniques used a global threshold value and were mostly studied on computer simulations of flat or spherical surfaces. Therefore, the conclusions derived may not be valid for freeform surface measurements. Moreover, an appropriate threshold value is dependent on the image characteristics, and the characteristics of an image from a freeform surface usually vary for each window. In this case, it is almost impractical to apply a predetermined global threshold value.

To tackle issues described above, we designed and investigated an adaptive centroid-finding algorithm after examine the four techniques' effects on the focal spot image during a real SHWS freeform surface measurement. The experimental results demonstrate the effectiveness of the proposed algorithm.

2. Centroid Finding in Freeform Surface Measurement

A. Noise

The measurement image has background noise that muddled the ability to distinguish focal spots. The noise does not follow a pattern and results from many factors, including the system arrangement and alignment.

The reflectors, for example, cause the interference pattern, or ghost image, shown in Fig. 1. Also, in the digital SHWS system, using a spatial light modulator (SLM) as a flexible lenslet array to better focus a wavefront with varying curvatures [15] increases the noise due to the zero and high-order diffraction.

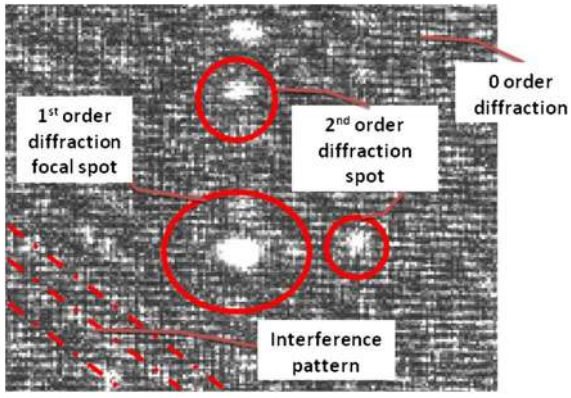

Fig. 1. (Color online) Image generated through the digital SHWS system with a mixture of focal spots and noisy signals.

B. Large Slope or Curvature

Freeform surfaces can have large slopes and/or slope changes (curvature). Because the image sensor is a plane, the focal spots may be distorted and/or out of focus, as shown in Fig. 2. Thus, the focal spot intensity and contrast would drop amidst the background noise, and detecting the spot would be difficult.

C. Variation of Image Characteristics

Because the measured surface is freeform, image characteristics, such as intensity distributions, signal-to-noise ratio, and focal spot shapes, can vary for each window.

Figures. 3(a) and 3(b) show a focal spot image sampled from a freeform surface and from a

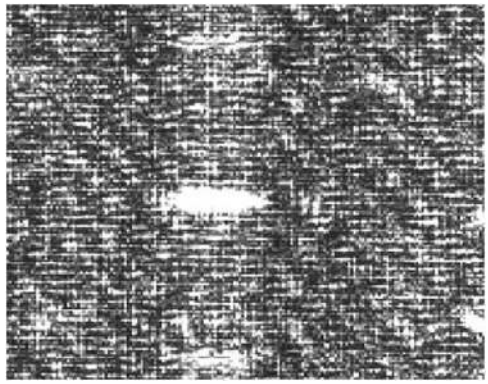

Fig. 2. Image generated through the SHWS system with a distorted focal spot at sample areas with large slope.

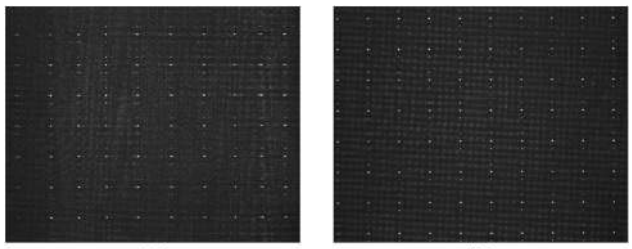

Fig. 3. Examples of focal spot image from (a) a freeform sample and (b) a reference plane mirror.

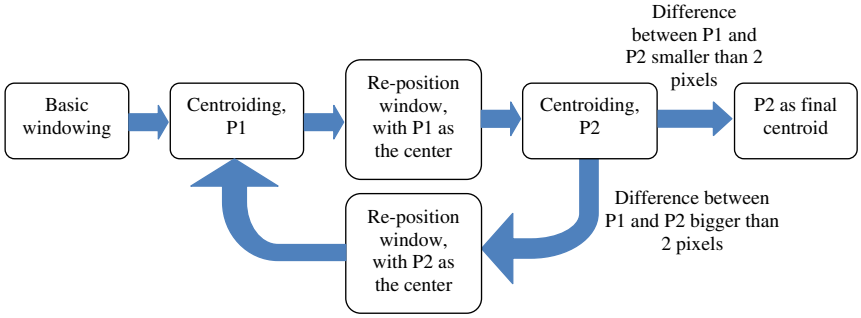

Fig. 4. (Color online) Flowchart of iteration applied to the centroiding process.

reference plane mirror, respectively. This comparison demonstrates that image characteristics can be inconsistent over the entire image for a freeform surface. For such images, a suitable global threshold value, which acts as a noise filter, is inaccurate for application to all windows.

3. Freeform Surface Measurements with Four Techniques

A. Thresholding, Power, Subwindowing, and Iteration

Thresholding excludes the contribution of low-intensity pixels. Increasing the power is elaborated

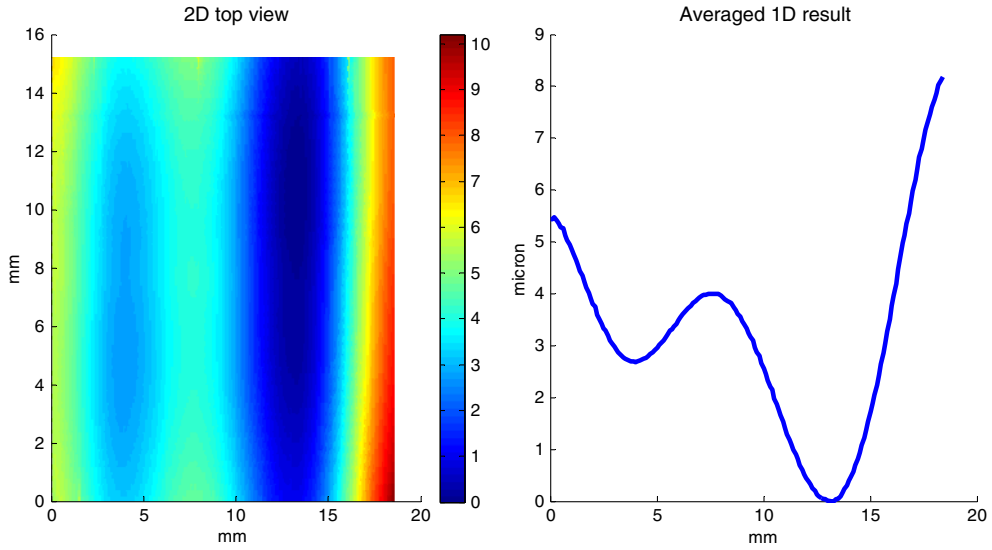

Fig. 5. (Color online) UA3P measurement results.

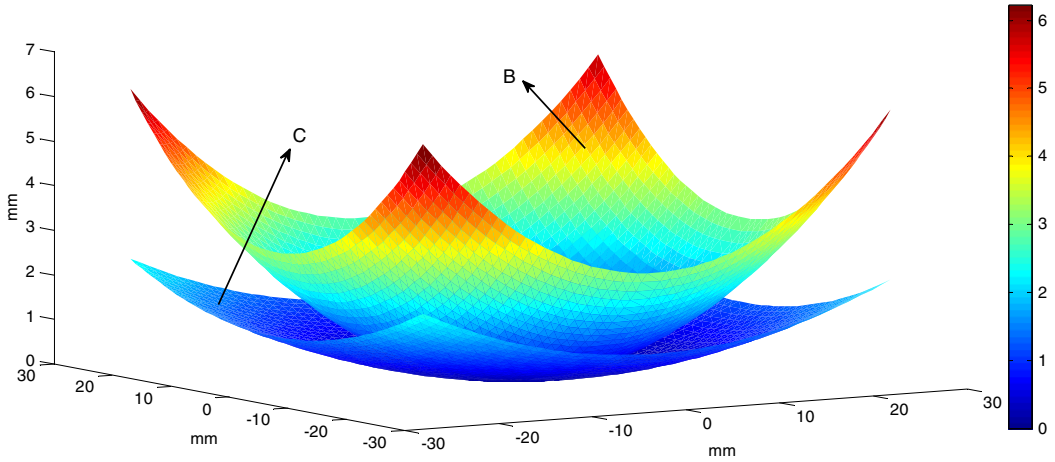

Fig. 6. (Color online) Profile of toroidal samples B and C.

Table 1. Specifications of Samples B and C

	Rx (mm)	Ry (mm)	Surface	Rx/Ry	Ry/Rx
B	100	107.2	Concave	0.933	1.072
C	245.4	276.6	Concave	0.887	1.127

by Eq. (2). Subwindowing is conducted so after the basic window is defined, we can reposition the window with the focal spot at its center. Iteration is normally implemented together with subwindowing. Figure 4 shows that iteration is applied until the difference between the subsequently calculated centroid and that of the basic window is less than a certain value (in this case, that value is 2 pixels).

$$I_{\text{new}} = I(X_i, Y_j)^{\alpha}. \tag{2}$$

According to previous studies [11–14], all four techniques work well to complement FMM. However, their effectiveness in freeform surface measurements is unknown. As such, this paper examined their performances in measuring a freeform sample.

B. Samples

There are three samples measured in this paper, labeled A, B, and C. Sample A has varying curvature over the measurement area. Figure 5 shows the measurement result from UA3P, a probing machine that specializes in measuring aspherical and freeform surfaces with nanoprecision [16]. Since the surface is not coated, the measured profile is the same as the wavefront profile at the sample surface.

Samples B and C (Fig. 6) are toroidal surfaces with different radii in two directions, and are manufactured from programmable diamond turning. These aspheric surfaces have wide applications in the optics and manufacturing industries [15]. Table 1 shows the detailed specifications of the two samples. Because both samples are not coated, the wavefront at the surface can be calculated from the specifications.

C. Experimental Investigation

A digital SHWS system was built up, as shown in Figs. 7 and 8. The HOLOEYE Photonics transmissive

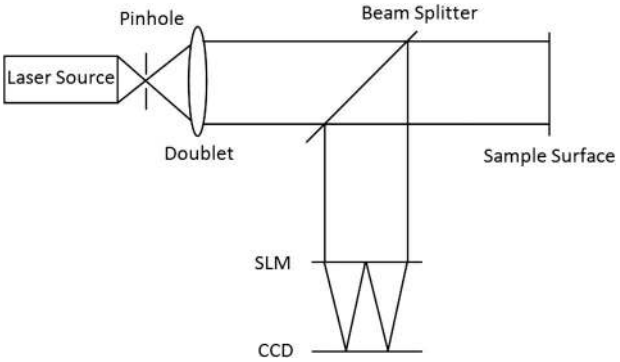

Fig. 7. (Color online) SHWS setup.

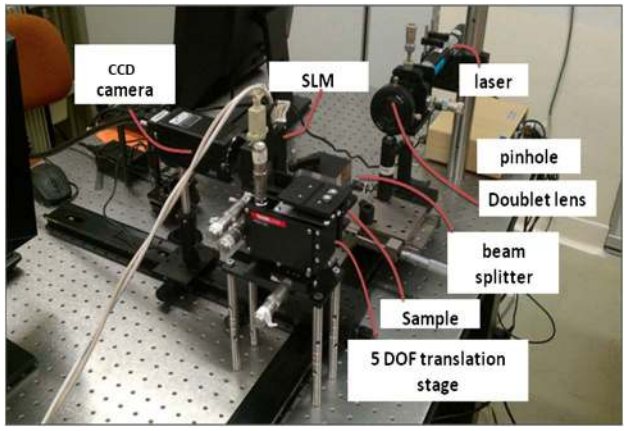

Fig. 8. (Color online) Experiment setup.

SLM has a pixel size of 32 μm [17]. The JAI CCD camera has a pixel size of 7.4 μm, and 4872 × 3248 resolution at 3.3 fps [18].

The focal spot image of the sample before and after a lateral shift is taken, and an eight-step scanning is conducted to increase the lateral resolution [19]. For sample A, each image has 12 × 10 windows (Fig. 9); the $f/\#$ of each simulated lenslet is 78.125. For sample B, each image has 14 × 9 windows (Fig. 10). For sample C, each image has 13 × 8 windows (Fig. 11). The $f/\#$ of each simulated lenslet in measuring both sample B and C is 39.0625. The wavefront is subsequently reconstructed from the curvature matrix calculated from the centroid displacement between the two [9].

Settings of different threshold values and varying powers, with the inclusion/exclusion of subwindowing and iteration, were experimentally investigated with sample A. In this paper, the RMS error (RMSE) of the measured wavefront, as listed in Table 2, is calculated against the UA3P measurement result. Note that the wavefront measured in the SHWS system is the one on the sampling plane. The RMSE value is not representative of the technique's accuracy,

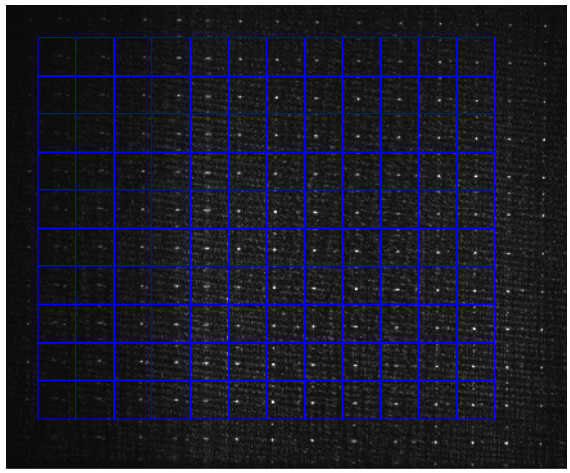

Fig. 9. (Color online) Focal spot image of sample A with 12 × 10 windows.

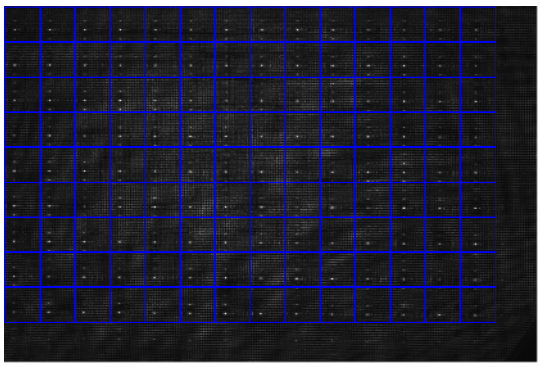

Fig. 10. (Color online) Focal spot image of sample B with 14 × 9 windows.

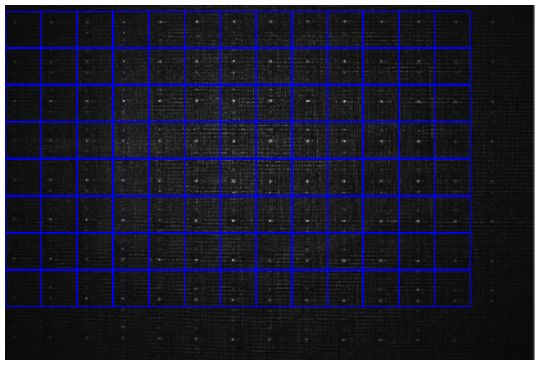

Fig. 11. (Color online) Focal spot image of sample C with 13 × 8 windows.

but only serves as an indicator to demonstrate the performance of various centroiding techniques. This is due to the scaling effect during wavefront propagation, sample repositioning, and mapping of sampling points in two measurement systems.

From Table 2, the smallest RMSE value is obtained at a threshold value of 50, a power of 3, without subwindowing and iteration. Figure 12 shows the corresponding reconstructed result. This setting, though optimum, is hardware dependent (i.e., changing a component could require a different setting for optimum performance).

Among the four techniques, thresholding has the greatest effect on the reconstructed surface. It is possible to obtain a satisfactory RMSE with a correct threshold value without including the other algorithms. If the threshold value is set to have a big gap from the satisfactory one, a high RMSE will be induced. The increment in RMSE cannot be rectified by the other techniques. This is true especially for regions with large slopes, where the corresponding image has focal spots with low intensity and weak contrast.

Figure 13(a), which is the result of wrong thresholding, has significant errors where the slopes are very large, because the algorithm fails to accurately detect the centroid positions. Figure 13(b) shows that even after incorporating power, subwindowing, and iteration techniques with the same thresholding, there is no improvement in the results.

Table 1 also shows that the power value is effective in improving the reconstruction accuracy only at

Table 2. RMSE Values for Various Settings

		RMSE (μm)		
Threshold	Power	Without Subwindowing	With Subwindowing	With Subwindowing and Iteration
0 (Without Thresholding)	1	0.8645	0.8928	0.8986
	3	0.8783	0.8560	0.6245
	5	0.3027	0.2990	0.2916
	10	0.2884	0.2885	0.2935
	15	0.2900	0.2900	0.2927
50	1	0.5456	0.3887	0.3399
	3	0.2443	0.2561	0.2851
	5	0.2820	0.2850	0.2948
	10	0.2897	0.2902	0.2929
	15	0.2905	0.2907	0.2925
100	1	0.2827	0.3165	0.3213
	3	0.3058	0.3136	0.3156
	5	0.3090	0.3120	0.3130
	10	0.3102	0.3112	0.3117
	15	0.3104	0.3111	0.3115
150	1	0.4842	0.4866	0.4868
	3	0.4811	0.4819	0.4820
	5	0.4806	0.4812	0.4812
	10	0.4806	0.4810	0.4810
	15	0.4806	0.4809	0.4809
200	1	0.5955	0.5958	0.5957
	3	0.5949	0.5951	0.5951
	5	0.5949	0.5950	0.5950
	10	0.5948	0.5949	0.5949
	15	0.5948	0.5949	0.5949

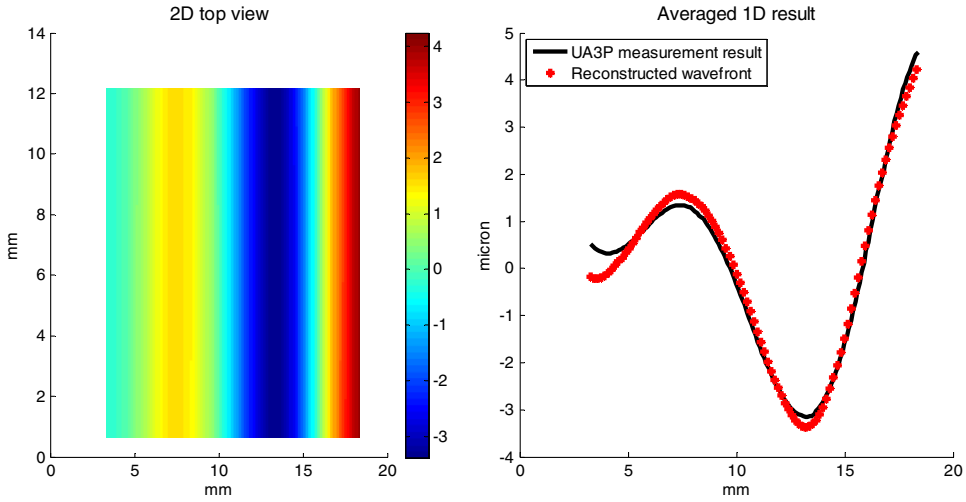

Fig. 12. (Color online) Measurement results at the best centroiding setting.

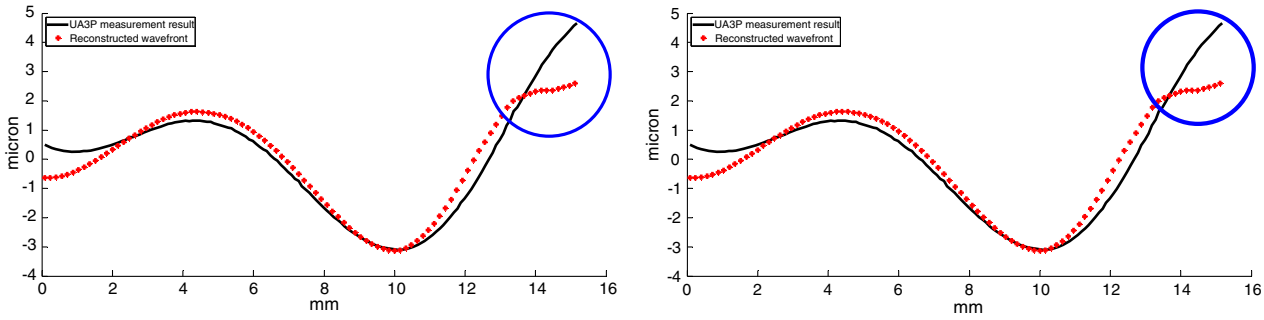

Fig. 13. (Color online) Reconstructed wavefront with a threshold value of 200, (a) power of 1, no subwindowing or iteration and (b) power of 15, subwindowing and iteration.

lower threshold values. Without thresholding, for example, a power of 10 decreases the RMSE from 0.8645 to 0.2884 μm. The accuracy improvement diminishes with increased power and eventually plateaus beyond a certain power value.

Table 2 also shows that the subwindowing and iteration techniques do not significantly improve accuracy and may even be slightly detrimental in certain settings.

4. Adaptive Centroid-Finding Algorithm for Freeform Surface Measurements

A. Adaptive Centroid-Finding Algorithm

The importance of thresholding has been demonstrated in the previous experiment; indeed, it is necessary to define an appropriate threshold value. Because an appropriate threshold value is dependent on the image characteristics, it is impractical to apply a global threshold value for all windows for freeform surface measurements. To address this issue, this paper proposes an adaptive centroid-finding algorithm. The proposed algorithm uses the local threshold value for each window, which is defined

Table 3. RMSE Values for Various Settings of Adaptive Centroid Finding

	Power	1	3	5	10	15
RMSE (μm)	Without iteration	0.3112	0.2969	0.2936	0.2924	0.2923
	With iteration	0.3173	0.2971	0.2937	0.2924	0.2923

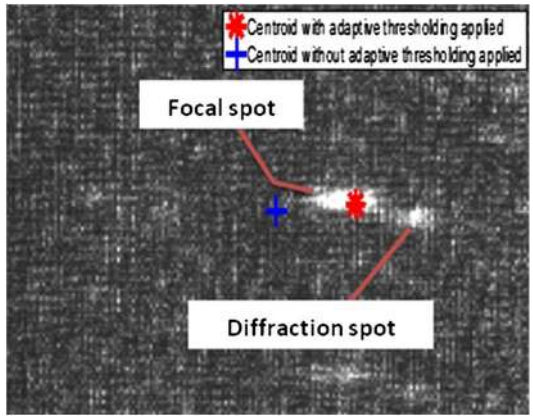

Fig. 14. (Color online) Centroid positions found with and without local thresholding at power 1 and no iteration. The threshold value is 0 when global thresholding is conducted.

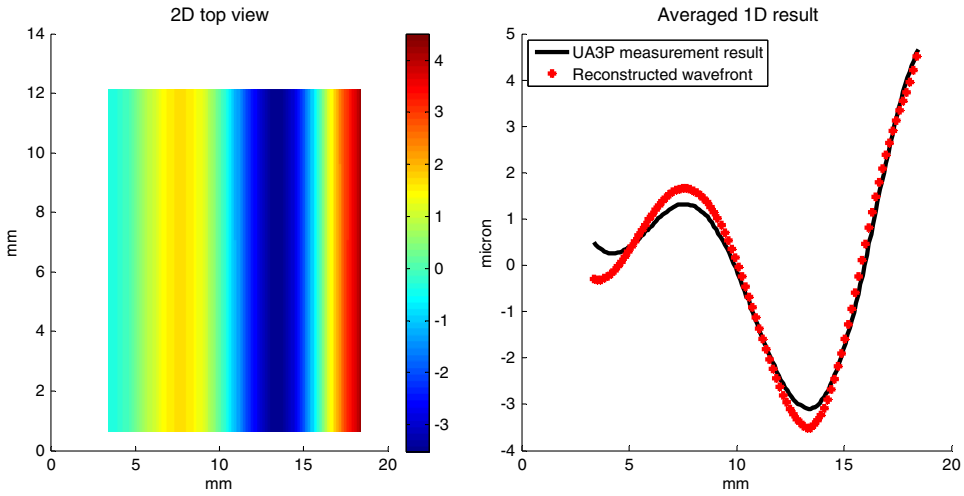

Fig. 15. (Color online) Measurement results with the implementation of the adaptive centroid-finding algorithm, at power 15 and no iteration.

individually by the local average intensity. Power is added to the new intensity map after local thresholding. The algorithm is shown in Eq. (3):

$$\begin{cases} I_{\text{thresh}} = \frac{\sum_{i=1}^{M}\sum_{j=1}^{N} I(X_i,Y_j)}{MN} \\ I_{\text{new}}(X_i,Y_j) = \begin{cases} 0, I(X_i,Y_j) <= I_{\text{thresh}} \\ I(X_i,Y_j) - I_{\text{thresh}}, I(X_i,Y_j) > I_{\text{thresh}} \end{cases} \\ X_C = \frac{\sum_{i=1}^{M}\sum_{j=1}^{N} X_i I_{\text{new}}(X_i,Y_j)}{\sum_{i=1}^{M}\sum_{j=1}^{N} I_{\text{new}}(X_i,Y_j)}, \quad Y_C = \frac{\sum_{i=1}^{M}\sum_{j=1}^{N} Y_j I_{\text{new}}(X_i,Y_j)}{\sum_{i=1}^{M}\sum_{j=1}^{N} I_{\text{new}}(X_i,Y_j)} \end{cases} \tag{3}$$

B. Experiment Results

The adaptive centroid-finding algorithm with varying power values and the inclusion/exclusion of iteration was tested on the set of experimental measurements of sample A used in the prior section. Table 3 shows the RMSE results.

From Table 3, it is clear that adaptive centroid finding can attain a satisfactory degree of accuracy. Even at regions with large slopes, the algorithm can identify the centroid position accurately (Fig. 14). Table 3 also shows that increasing the power and iteration contribute little to improve the accuracy of the results. Figure 15 shows the reconstructed results at power 15, without iteration.

When an optimized global thresholding is applied in sample B (Fig. 16), the RMSE of the reconstructed wavefront is 0.037 μm. Implementing the adaptive centroid-finding algorithm reduces the RMSE to 0.010 μm.

When an optimized global thresholding is applied in sample C (Fig. 17), the RMSE of the reconstructed

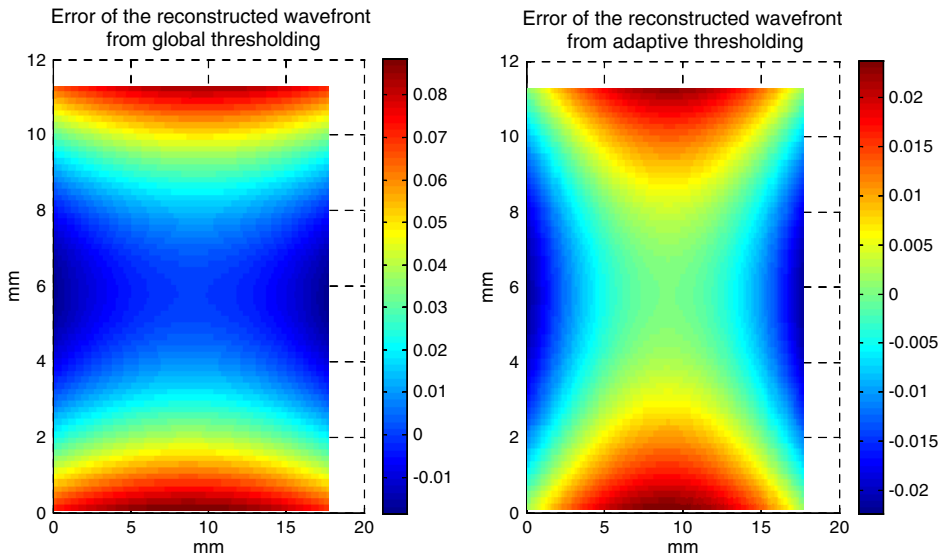

Fig. 16. (Color online) Error of the reconstructed wavefront of sample B obtained through the global threshold centroid-finding algorithm, and adaptive threshold centroid finding.

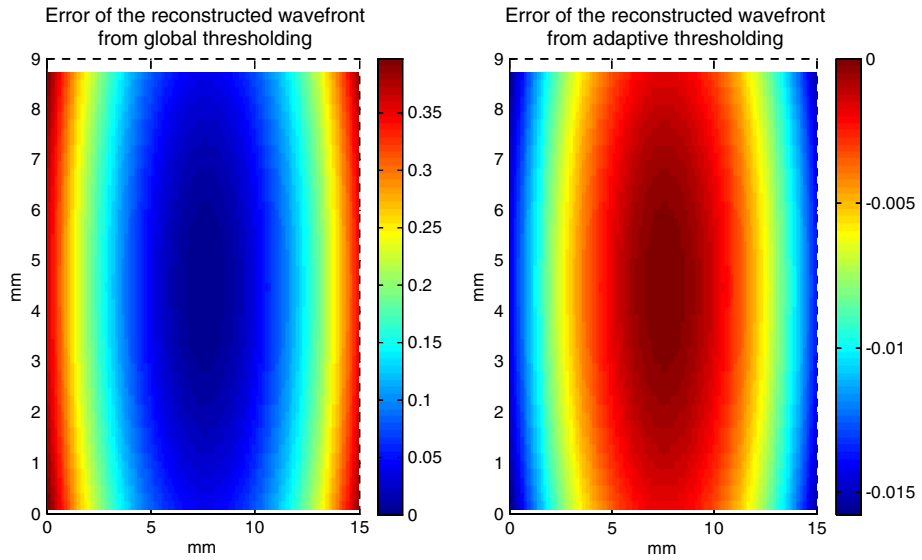

Fig. 17. (Color online) Error of the reconstructed wavefront of sample C obtained through global threshold centroid-finding algorithm and adaptive threshold centroid finding.

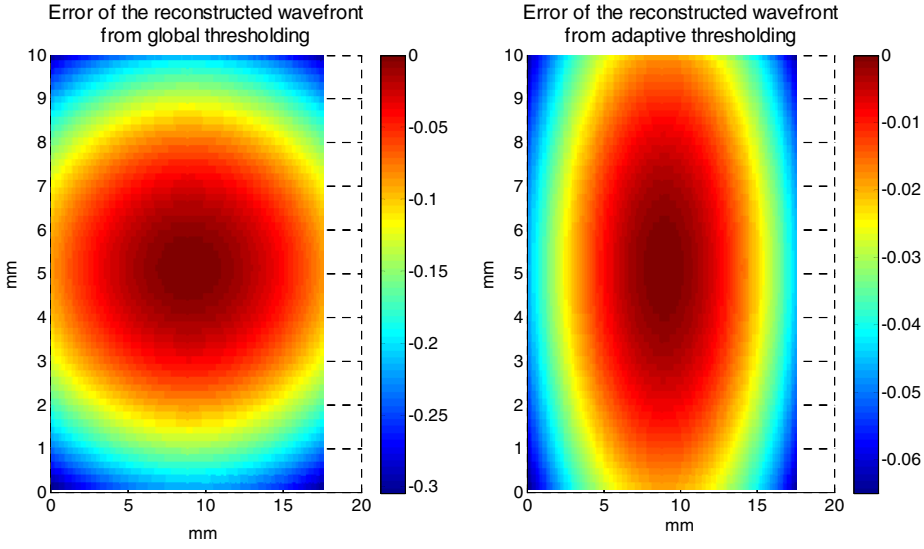

Fig. 18. (Color online) Error of the reconstructed wavefront of sample C obtained through the global threshold centroid-finding algorithm, and adaptive threshold centroid finding, in a conventional SHWS system.

wavefront is 0.173 μm. Implementing the adaptive centroid-finding algorithm reduces the RMSE to 0.007 μm.

To verify the general validity of the proposed centroiding algorithm, toroidal sample C also is measured in the conventional SHWS system, with the same setting used in the design of the SLM. Figure 18 shows that the RMSE resulting from the implementation of the global thresholding technique is 0.126 μm. When the adaptive centroiding algorithm is applied, the error reduces to 0.027 μm.

The measurement results of the three samples demonstrate the effectiveness of the proposed algorithm with the consideration of local thresholding.

5. Conclusion

For freeform surface measurements, the conventional centroid-finding algorithms with global thresholding cannot accurately determine the centroid positions. An appropriate threshold value is dependent on the image characteristics, which usually vary over the entire image. Because of these results, an adaptive centroid-finding algorithm is proposed that uses local threshold values defined by the local average intensity instead of a global value. Through experimental investigation of three freeform surfaces, we have proven the feasibility and effectiveness of the proposed algorithm. As such, adaptive centroid finding is recommended for freeform surface measurements.

This project is supported by National Metrology Center (NMC), A*STAR, Singapore. The authors would like to thank Prof Ping Koy Lam from the Australian National University for providing the samples.

References

1. X. Jiang, P. Scott, and D. Whitehouse, "Freeform surface characterization—a fresh strategy," CIRP Ann. **56**, 553–556 (2007).
2. R. Henselmans, Non-Contact Measurement Machine for Freeform Optics (Ph.D Thesis, Technische Universiteit Eindhoven, 2009).
3. B. C. Platt and R. Shack, "History and principles of Shack–Hartmann wavefront sensing," J. Refract. Surg. **17**, 573–577 (2001).
4. D. Malacara, *Optical Shop Testing*, 3rd ed. (Wiley, 2007).
5. J. C. Wyant, "Advances in interferometric surface measurement," Proc. SPIE **6024**, 602401 (2005).
6. Spiricon, Inc., "Hartmann wavefront analyzer tutorial," (2004), http://www.spiricon.com.
7. R. Schmitt, I. Jakobs, and K. Vielhaber, "Wavefront sensor design based on a micro-mirror array for a high dynamic range measurement at a high lateral resolution," *New Optical Sensors and Measurement Systems* (Springer, 2009), pp. 628–633.
8. S. Rios and D. Lopez, "Interferometric Shack–Hartmann wavefront sensor using an array of superresolution pupil filters," Appl. Opt. **49**, 2334–2338 (2010).
9. L. Zhao, W. Guo, X. Li, and I-M. Chen, "Reference-free Shack–Hartmann wavefront sensor," Opt. Lett. **36**, 2752–2754 (2011).
10. Ai-li Xia and C.-w. Ma, "An improved centroid detection method based on higher moment for Shack–Hartmann wavefront sensor," Proc. SPIE **7850**, 78501Q (2010).
11. A. Vyas, M. B. Roopashree, and B. R. Prasad, "Optimization of existing centroiding algorithms for Shack–Hartmann sensor," *Proceedings of the National Conference on Innovative Computational Intelligence & Security Systems* (2009), pp. 400–405.
12. A. Vyas, M. B. Roopashree, and B. R. Prasad, "Performance of centroiding algorithms at low light level conditions in adaptive optics," *Proceedings of the International Conference on Advances in Recent Technologies in Communication and Computing* (2009), pp. 366–369.
13. Z. Jiang, S. Gong, and Y. Dai, "Monte Carlo analysis of centroid detected accuracy for wavefront sensor," Opt. Laser Technol. **37**, 541–546 (2005).
14. X. Yin, L. Zhao, X. Li, and Z. Fang, "Automatic centroid detection and surface measurement with a digital Shack–Hartmann wavefront sensor," Meas. Sci. Technol. **21**, 015304 (2010).
15. L. P. Zhao, N. Bai, and X. Li, "Asymmetrical optical lenslet array realized by spatial light modulator for measuring toroidal surfaces," Appl. Opt. **47**, 6778–6783 (2008).
16. Panasonic, http://industrial.panasonic.com/ww/products_e/product_cat2/ADAH000_e/ADAH000_e/index.html.
17. HOLOEYE Photonics, http://www.holoeye.com/spatial_light_modulator_lc_2002.html.
18. JAI, http://www.jai.com/en/products/am-1600cl.
19. W. Guo, L. Zhao, X. Li, and I-M. Chen, "Optimization of scanning strategy of digital Shack–Hartmann wavefront sensing," Appl. Opt. **51**, 121–125 (2012).